Precise and Automatic 3-D Absolute Geolocation of Targets Using Only Two Long-Aperture SAR Acquisitions

Sergi Duque, Alessandro Parizzi[ID], and Francesco De Zan[ID]

Abstract— This paper deals with precise absolute geolocation of point targets by means of a pair of high-resolution synthetic aperture radar (SAR) acquisitions, acquired from a satellite. Even though a single SAR image is a 2-D projection of the backscatter, some 3-D information can be extracted from a defocussing analysis, depending on the resolution, thanks to orbital curvature. A second acquisition, observing the same scene under a different look angle, adds stereogrammetric capability and can achieve geolocation accuracy at decimeter level. However, for the stereogrammetric analysis to work, it is necessary to match targets correctly in the two images. This task is particularly difficult if it has to be automatic and targets are dense. Unfortunately, the defocussing-based geolocation is not sufficient for reliable target matching: the limiting factor is the unknown tropospheric delay that can cause geolocation errors of several meters in the elevation direction. However, observing that the tropospheric phase screen displays a low-pass character, this paper shows how to identify statistically the local atmospheric disturbances, therefore dramatically improving the score of successful matching. All steps involved exploit peculiar radar image characteristics and, thanks to this, avoid generic point cloud matching algorithms. The proposed algorithm is shown at work on a pair of TerraSAR-X staring spotlight images.

Index Terms— 3-D point cloud, crossing orbit, high resolution, satellite geodesy, stereogrammetry, synthetic aperture radar (SAR), target matching, urban digital elevation model (DEM), zenith path delay (ZPD) estimation.

I. INTRODUCTION

THEORETICAL studies and first airborne experiments on synthetic aperture radar (SAR) radargrammetry were carried out during the 1960s and 1970s [1]–[3] and were mainly oriented toward retrieving digital elevation models (DEMs). Because of the spatial resolution of the first SAR civilian satellites in the 1980s and 1990s, the obtained height accuracy by radargrammetric techniques was in the order of several meters [4], [5], far away from the few meters that could be obtained by InSAR techniques [6]–[8]. Permanent scatterer interferometry (PSI), introduced in [9], proved to be able to exploit interferometrically the full spatial resolution of the SAR images by limiting the measurements to point targets; consequently, it found wide application in urban scenarios. The technique took advantage of the increasing amount of available acquisitions and used image stacks to estimate ground deformation and topography. The first urban accurate DEM using PSI was shown in [10]. This work reached an absolute 3-D accuracy below 1 m by means of ground control points and three different stacks with more than 200 acquisitions in total.

ENVISAT and ALOS PALSAR showed an improvement in orbit accuracy with respect to previous European Remote Sensing Satellites. It was possible to geocode a single SAR image with an absolute accuracy of few meters by using a DEM and refined orbits [11]. The launch of very-high-resolution (VHR) sensors with precise orbit knowledge, such as TerraSAR-X and COSMO-SkyMed, has boosted again the interest in stereo-SAR [12]–[15]. In [16], SAR imagery from COSMO-SkyMed, TerraSAR-X, and RADARSAT-2 was geolocated after applying several earth-system effects showing a significant geolocation accuracy improvement. Recent works [17], [18] are focused on the possibility of locating a point in the SAR image given its ground 3-D position and applying a set of geodynamic and path delay corrections. These two works show the potentiality of using TerraSAR-X acquisitions for precise geolocation at the centimeter level. Precise absolute geolocation has been also applied to recent ESA SAR satellite mission Sentinel-1. The work developed in [19] shows that when geodynamic and atmospheric path delays are taken into account, the geolocation accuracy is significantly improved with respect to nominal product specifications. In [20], geodesy and tomography are fused to create a dense point cloud with absolute positioning accuracy at the submeter level. In order to achieve this accuracy, four different stacks were processed and the targets to be used as control points were selected manually.

At present, obtaining an absolute 3-D point cloud using spaceborne SAR imagery presents the following limitations.

1) A need for a large set of images. This may imply a huge economic cost and also requires time to acquire the images.
2) For an accurate absolute 3-D geolocation, the extra signal path delay due to traveling through media different than vacuum (i.e., the atmosphere) needs to be taken into account. This implies the necessity of external data

to estimate the ionospheric and tropospheric delays seen by the sensor geometry.

3) Techniques based on SAR radargrammetry present problems to automatically identify the point targets within the different employed geometries.

The method in this paper uses as input the height–tropospheric delay relationship derived from the autofocus analysis described in [21]. These inputs and the assumption of a low spatial variation of the tropospheric delay at a certain fixed height are the key points to carry out the automatic matching and to find the absolute 3-D positioning and tropospheric delays. The proposed method solves the previously raised problems as follows.

1) It only needs a minimum number of two images acquired with different geometries. This means first of all a reduced cost and a reduced acquisition time span that can be under a week even with current spaceborne SAR systems.

2) The proposed technique estimates the path delays with no need for external information.

3) The proposed technique identifies automatically point targets in the two imaging geometries, based solely on radar signal properties. In particular, there is no need for matching algorithms like those used in computer vision.

The price to pay with respect to other techniques is a reduced accuracy, in the order of a few tens of centimeters, which is explained by the use of just two acquisitions. SAR tomography and radargrammetry that exploit a larger set of VHR images reach the centimeter level in geolocation accuracy. The density of selected points by the proposed technique may be lower than the previously mentioned methods. Finally, the last drawback of the method described here is the need of very long spaceborne SAR apertures, such as the ones present in TerraSAR-X Staring Spotlight (ST) data. This means that the observed area on the ground is limited to a few square kilometers.

II. SINGLE-IMAGE PROCESSING

Duque *et al.* [21] studied the dependence of azimuth defocussing on target height for spaceborne SARs. This effect can be considered negligible for short apertures (a few kilohertz). However, for a large azimuth bandwidth, if the assumed focusing height is wrong, the image will present a significant blurring effect. For example, in a TerraSAR-X Staring ST acquisition with an incidence angle of 47°, the peak of a point target is 60% wider than the nominal resolution when the target is focused assuming a height error of 100 m. Therefore, the estimation of the residual phase curvature (frequency modulation (FM) rate in the following) for a given point target is linked to the difference between the target height and the height used in focusing. In case the reader is interested in detailed performance analysis of the residual FM rate estimation, this is discussed in Appendix A. A different number of effects that contribute to an FM rate mismatch were discussed in [21]. Further details and extension of these effects can be found in Appendix B. In this paper, the approach used to estimate the height from FM rate mismatch is an autofocus by repeated focusing: the image is processed assuming different
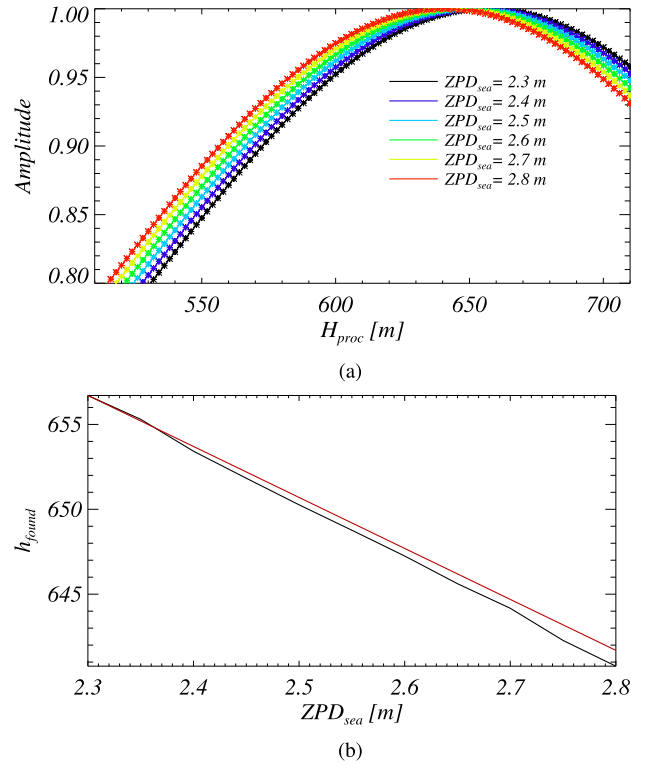

Fig. 1. (a) Amplitude function for different assumed ZPDs in processing and (b) height found for different ZPDs. Black line: data. Red line: analytical slope.

heights and the amplitude of each point target is monitored as a function of height. The correct height for each target is the one corresponding to the maximum amplitude. Apart from height error, the other main contributors to FM rate mismatch are the tropospheric delay. Indeed, the autofocus processing is carried out varying two parameters, the height processing and the assumed zenith path delay (ZPD), at the sea level. The impact of height and the tropospheric delay in the focusing cannot be separated with a single-image processing. Thus, the height is estimated as a function of the assumed tropospheric delay by

$$h = h_{\text{ZPD}_{\text{ref}}} + \kappa \cdot \Delta \text{ZPD} \tag{1}$$

where $h_{\text{ZPD}_{\text{ref}}}$ being the obtained autofocus height at a reference ZPD and κ being the parameter linking height and ZPD. Fig. 1(a) shows, for a point target, the resulting amplitude with respect to the focusing height for different assumed ZPDs at the sea level. The obtained height for different ZPDs is plotted in Fig. 1(b) in black and a derived analytical expression is plotted in red. The derivation details of this analytical expression can be found in Appendix B. Here, it has been calculated assuming acquisition's incidence angle and TerraSAR-X orbit parameters.

III. TWO-IMAGE INVERSION

This section presents the joint exploitation of the previously discussed autofocus method and stereogrammetry. The combined method requires two images acquired with long apertures and with significant incidence angle discrepancy. The flowchart in Fig. 2 shows that the input consists of two
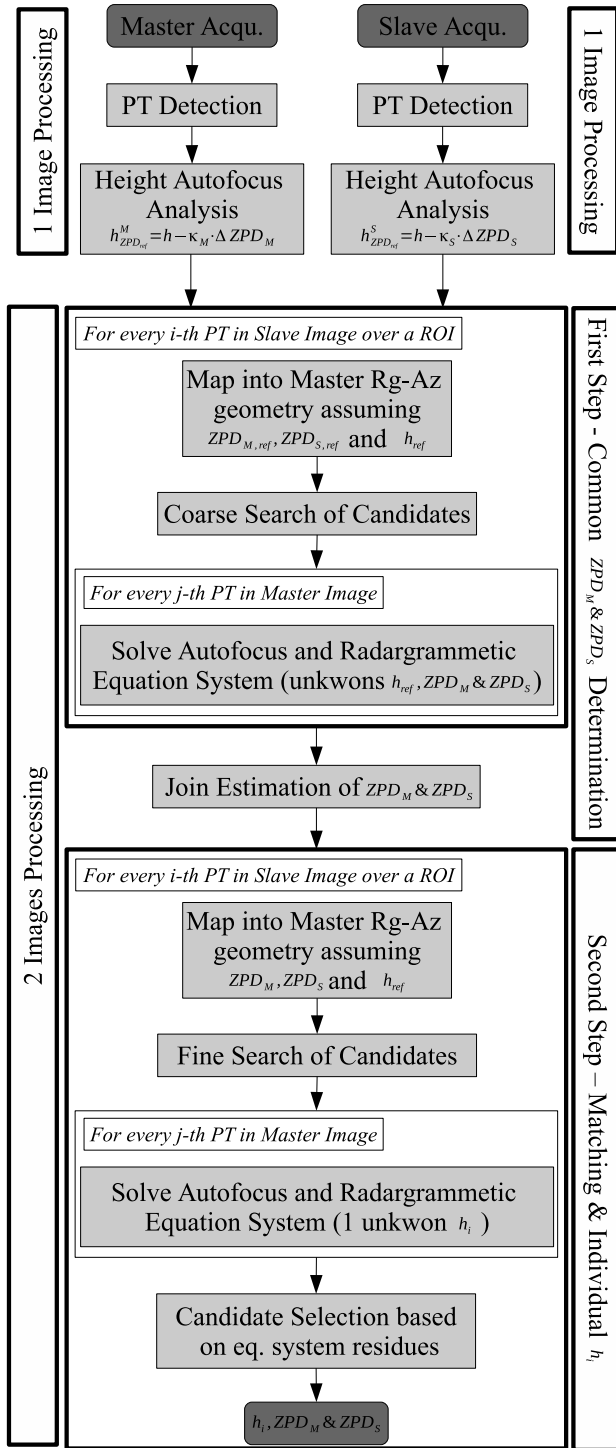
This article has been accepted for inclusion in a future issue of this journal. Content is final as presented, with the exception of pagination.

DUQUE *et al.*: PRECISE AND AUTOMATIC 3-D ABSOLUTE GEOLOCATION OF TARGETS
3

Fig. 2. Processing flowchart.

not show a clear pattern as well as cells with more than one dominant target. Some cells may be close to show a pointlike target behavior and they pass the target selection. This can happen because of different reasons such as it may happen when its scattering mechanism is not exactly a pointlike target. Another reason could be that there is another target close by that interferes in the target response. In those cases, the height estimation error will be higher than the expected according to the target's SCR. A key point of the method is the hypothesis that the ZPD can be considered constant within a given region of interest (ROI). The atmospheric delay in the horizontal plane is expected to present a correlation length of a few kilometers [22]. This assumption is widely used in PSI techniques [9]. Therefore, it is reasonable to choose an ROI with a length of few hundred of meters and to assume that at the defined height the atmospheric delay is constant.

The two-image processing is divided into two steps. The first step retrieves the ZPDs within the ROI for both acquisitions. The second step matches slave targets to the corresponding master targets and estimates the absolute heights at the same time.

A. Step I. Estimation of ZPD_M and ZPD_S

Each point target is mapped into the master geometry assuming the reference ZPDs for the master and slave acquisitions ($ZPD_{M,\mathrm{ref}}$ and $ZPD_{S,\mathrm{ref}}$), and target height in the slave image obtained from the autofocus at $ZPD_{S,\mathrm{ref}}$. Let us assume the same ZPD reference for master and slave acquisitions, i.e., $ZPD_{\mathrm{ref}} = ZPD_{M,\mathrm{ref}} = ZPD_{S,\mathrm{ref}}$. Thus, the range and azimuth differences between the observed target position in the master and the projected position from the slave are ascribable to discrepancies of the true height and tropospheric delays with respect to the assumed references, plus some measurement error. The target in the master geometry will appear within a region around the projected position. The boundaries of this region can be reasonably established taking into account the accuracy of the height estimation in slave geometry and reasonable range of ZPDs values for master and slave acquisitions. All targets falling inside this region are the candidates to be the correct match. This is referred in the scheme shown in Fig. 2 as *"Coarse Search of Candidates."* It is possible to formulate a system of equations for every candidate. Two equations are related to stereoradargrammetry and the other two to the autofocus process for each image, as a function of height and tropospheric delay. The unknowns are the target's height and the two tropospheric delays of the acquisitions. Therefore, we have a system of four linear independent equations and three unknowns. Following the flowchart depicted in Fig. 2, the system of equations is solved for every candidate of each projected target.

1) Radargrammetric Equations: Fig. 3 shows the master and slave geometries, where R_M and R_S are the master and slave ranges, A_M and A_S represent the azimuth positions, θ_M and θ_S refers to the master and slave incidence angles, and α is the heading angle difference between both trajectories.

independent autofocus analyses from the two acquisitions. One acquisition geometry will be set as a reference, named from now on the master acquisition; on the other hand, the other geometry, the slave acquisition, will be projected on it. For each image, there is a point target selection. This point target selection is done selecting the local maxima of the points that are above a certain signal-to-clutter ratio (SCR). Then, those points are checked that they follow a clear "amplitude versus height processing" pattern, like the one shown in Fig. 1(a), to estimate their height. Targets that are not point targets do

This article has been accepted for inclusion in a future issue of this journal. Content is final as presented, with the exception of pagination.

4   IEEE TRANSACTIONS ON GEOSCIENCE AND REMOTE SENSING
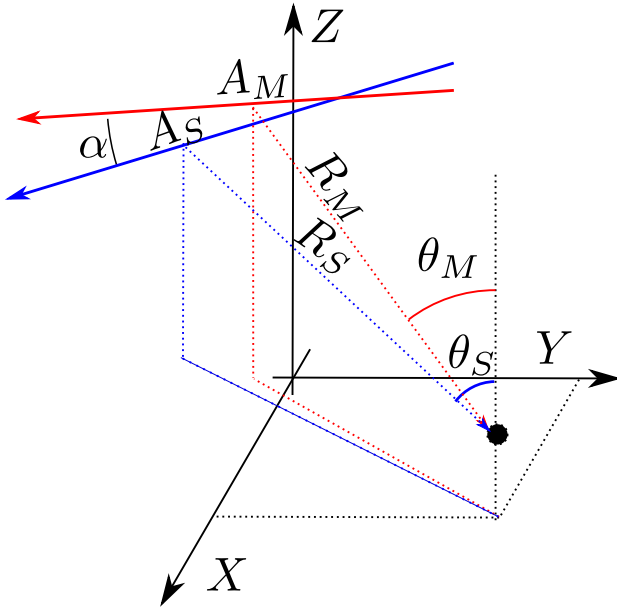
Fig. 3.   Stereoradargrammetric acquisition scheme.

The projected slave coordinates into the master geometry can be expressed by

$$R_{S \to M} = R_S \cos(\alpha) \cdot \frac{\sin(\theta_M)}{\sin(\theta_S)} - A_S \sin(\alpha) \cdot \sin(\theta_M)$$
$$A_{S \to M} = A_S \cos(\alpha) + R_S \sin(\alpha) \cdot \sin(\theta_S). \qquad (2)$$

Note that here the incidence angles, θ_M and θ_S, are calculated assuming a reference height. The radargrammetric equations come from the position difference between the projected target and the candidate, that is,

$$\Delta R = R_M - R_{S \to M}$$
$$\Delta A = A_M - A_{S \to M}. \qquad (3)$$

They are related to the height and tropospheric differences by

$$\Delta R = a \cdot \Delta h + b \cdot \Delta ZPD_S + c \cdot \Delta ZPD_M$$
$$\Delta A = d \cdot \Delta h + e \cdot \Delta ZPD_S \qquad (4)$$

where Δh, ΔZPD_M, and ΔZPD_S are the height, the master, and slave tropospheric ZPD differences with respect to the assumed references, respectively. The coefficients are approximately

$$a \approx \frac{\sin(\Delta \theta)}{\sin(\theta_S)} \cos(\alpha) \quad d \approx \frac{\sin(\alpha)}{\tan(\theta_S)}$$
$$b \approx \frac{-\sin(\theta_M)}{\sin(\theta_S)} \frac{\cos(\alpha)}{\cos(\theta_S)} \quad e \approx \frac{-\sin(\alpha)}{\sin(\theta_S) \cos(\theta_S)}$$
$$c \approx \frac{\cos(\alpha)}{\cos(\theta_M)}. \qquad (5)$$

In practice, the coefficients are calculated numerically for every selected point target.

2) Autofocus Equations: The other two equations are related to the defocus dependence on height and ZPD of both acquisitions. Following (1), they can be expressed as

$$h^M_{ZPD_{ref}} = h - \kappa_M \cdot \Delta ZPD_M$$
$$h^S_{ZPD_{ref}} = h - \kappa_S \cdot \Delta ZPD_S \qquad (6)$$

where κ_M and κ_S are the link parameters between height and ZPD for master and slave acquisitions, respectively, $h^M_{ZPD_{ref}}$ and $h^M_{ZPD_{ref}}$ are the obtained autofocus heights assuming the reference ZPD in master and slave, and finally, h is the true height of the target.

3) Equation System: At this point, the whole problem can be modeled as a linear system of equations as

$$D = M \cdot X. \qquad (7)$$

where D is the measured data vector, M is the system matrix, and X is the unknowns vector containing the true height of the target and the two ZPDs differences with respect to the assumed reference. The measured data vector and the unknown vector are defined as follows:

$$D = \begin{pmatrix} \Delta R + a \cdot h_{ref} \\ \Delta A + d \cdot h_{ref} \\ h^M_{ZPD_{ref}} \\ h^S_{ZPD_{ref}} \end{pmatrix} \text{ and } X = \begin{pmatrix} h \\ \Delta ZPD_M \\ \Delta ZPD_S \end{pmatrix}. \qquad (8)$$

The design matrix M is

$$M = \begin{pmatrix} a & b & c \\ d & 0 & e \\ 1 & -\kappa_M & 0 \\ 1 & 0 & -\kappa_S \end{pmatrix}. \qquad (9)$$

The system of equations is solved for all targets and all possible matches, and the ZPD solutions are collected in a 2-D histogram. All the equation systems formed from good matches yield consistent solutions in terms of ZPDs, i.e., one for master and one for slave, within the corresponding error intervals. A wrong match would imply the misinterpretation of the spatial separation between targets in the two geometries as height (stereoeffect) and, consequently, a wrong interpretation of the atmospheric contribution. Hence, the equations related to the bad candidates (wrong matches) produce almost random ZPD solutions. Following these premises, the algorithm picks the ZPD's pair corresponding to a robust estimation of the 2-D ZPD distribution mean.

B. Step II. Automatic Matching and Height Determination

Once the ZPDs have been estimated for the ROI, it is possible to rewrite again the system of equations taking just the height as unknown. Following a process similar to the previous step, every target from the slave image is projected into master geometry. This time the obtained ZPDs will be used for the projection together with the height derived from slave autofocus taking into account ZPD_S, i.e., $h^S_{ZPD_S}$. Therefore, the position differences between the target in master and projection are mainly due to the relatively large height error in the autofocus estimation. Small discrepancies can also occur due to small positioning errors and ZPD's relative accuracy. Since the ZPDs are set, now the search area for the candidates is just defined by the relative ZPDs accuracy and the height autofocus accuracy. This is highlighted in flowchart shown in Fig. 2 as *"Fine Search of Candidates."* Note that this fine search area does not need to take into account orbit errors since they are already intrinsically included in the absolute ZPD estimation.

This article has been accepted for inclusion in a future issue of this journal. Content is final as presented, with the exception of pagination.

DUQUE *et al.*: PRECISE AND AUTOMATIC 3-D ABSOLUTE GEOLOCATION OF TARGETS

5

The system of equations from (7) is reformulated with the unknown vector, X', containing just the height, and the previous system design matrix, M', is now a vector. Therefore, D' and X' are expressed as

$$D' = \begin{pmatrix} \Delta R + a \cdot h_{\mathrm{ZPD}_S}^S \\ \Delta A + d \cdot h_{\mathrm{ZPD}_S}^S \\ h_{\mathrm{ZPD}_M}^M \\ h_{\mathrm{ZPD}_S}^S \end{pmatrix} \text{ and } X' = (h) \qquad (10)$$

and

$$M' = \begin{pmatrix} a \\ d \\ 1 \\ 1 \end{pmatrix} \qquad (11)$$

where $h_{\mathrm{ZPD}_M}^M$ and $h_{\mathrm{ZPD}_S}^S$ are the heights derived from the autofocus analysis in master and slave acquisitions taking into account the previously obtained ZPDs. In case that more than one target falls within the *"Fine Search of Candidates,"* the automatic matching selects the most likely one. This is carried out by analyzing the weighted residuals from the system of equations described in (7). The target with the smallest residuals will correspond most likely to the correct matching

$$d_M^2 = (D' - M' \cdot \hat{X}')^T \cdot C_{D'}^{-1} \cdot (D' - M' \cdot \hat{X}') \qquad (12)$$

where $C_{D'}$ is the measured data covariance matrix and $\hat{X}'$ is the new estimated unknowns vector.

IV. PERFORMANCE ANALYSIS

A. Equation System Sensitivity

In this section, we discuss the impact of different error sources on the estimation of the model parameters. The system of equations presented in (7) is solved by applying the weighted least-squares algorithm. The covariance of the measured data is estimated taking into account the accuracy of the target's range-azimuth positioning as well as the height accuracy obtained by the autofocus process. Note that if the trajectories are not parallel (i.e., $\alpha \neq 0$), the covariance matrix is not diagonal. The heading angle difference presents a dependency not only with the incidence angle difference but also with the orbit height and the ROI latitude. Acquisitions show no heading angle difference at the Equator. Thus, at latitudes around the Equator, the azimuth radargrammetric equation shows poor sensitivity, and the system of equations is ill-conditioned. We will assume the latitude of Berlin, 52.52°, for the following analysis. At this latitude and taking into account TerraSAR-X orbit, the ratio between the incidence angle variation and heading angle variation is 5.6. Fig. 4 shows the theoretical accuracy for a target with an SCR of 20 dB and taking into account the previous assumptions of flat earth and trajectories with no velocity component in the z-axis.

As expected and as shown in Fig. 4, it is not possible to properly retrieve the unknowns for small incidence angle differences between acquisitions. However, the variables present different behaviors with respect to acquisition geometries. The height accuracy improves with an increasing angle

TABLE I
VARIABLE AND SYSTEMATIC ERRORS FOR $\theta_M = 30°$ AND TWO DIFFERENT INCIDENCE ANGLES FOR SLAVE ACQUISITION, $\theta_S = 40°$ AND $\theta_S = 50°$

	$\theta_M = 30°$	
	$\theta_S = 40°$	$\theta_S = 50°$
σ_h	38.6 cm	33.5 cm
σ_{ZPD_M}	21.3 cm	22.7 cm
σ_{ZPD_S}	17.0 cm	12.9 cm
$\sigma_{h,sys}$	72.9 cm	42.6 cm
$\sigma_{ZPD_M,sys}$	9.8 cm	10.7 cm
$\sigma_{ZPD_S,sys}$	12.4 cm	10.6 cm

difference [Fig. 4(a)]. In addition, it can be observed that height accuracy is also better for steeper incidence angles. The larger the incidence angle is, the better the ZPDs are estimated, as shown in Fig. 4(c) and (d). This is mainly due to the larger integration path in the slant direction. Another factor is that the height obtained by the autofocus method at the reference ZPD presents better accuracy with larger angles. Consequently, the ZPD linked to the autofocus height by (6) also shows better accuracy for larger incidence angles. The combined error of both ZPD estimations is illustrated in Fig. 4(b). It is clear that this error depends mainly on the sum of both incidence angles instead of the difference, as it is on the height.

There are also error sources that can be considered constant for the whole ROI. The main systematic errors are orbit inaccuracy and autofocus height estimation biases (see Section V-A2 and, for further details, Appendix A). The inaccuracies for TerraSAR-X Science Orbit are in the order of few centimeters as demonstrated in [23]. We can reasonably assume them to be $\sigma_{Rg,orb} = 1.4$ cm, and $\sigma_{Az,orb} = 2.5$ cm, in range and azimuth. As it will be shown later (see Section V-A2), the autofocus height estimation presents systematic errors in the order of 3 m. Thus, taking into account these values, it is possible to derive the theoretical systematic errors for height and tropospheric delay estimations. Table I gives the random and systematic errors assuming an SCR of 20 dB, a master acquisition incidence angle of 30°, and two different incidence angles for slave acquisition, 40° and 50°.

It is not possible to eliminate the systematic errors, the only one can do is to characterize them. The absolute accuracy for height is still very good. The absolute height systematic error is below the meter for incidence angle separations above 10°.

B. Probability of Correct Automatic Matching

The accuracy in Section III was derived assuming that the target is properly identified in the master and slave acquisitions. In general, a target that does not correspond to the correct matching will have a larger statistical distance than the correct target. In order to analyze how likely is to choose the correct target, the authors have done a Monte Carlo simulation with two targets falling into the *"Fine Search of Candidates."* One corresponds to the correct target we want to match and the other to a different target from the master image

This article has been accepted for inclusion in a future issue of this journal. Content is final as presented, with the exception of pagination.

6   IEEE TRANSACTIONS ON GEOSCIENCE AND REMOTE SENSING
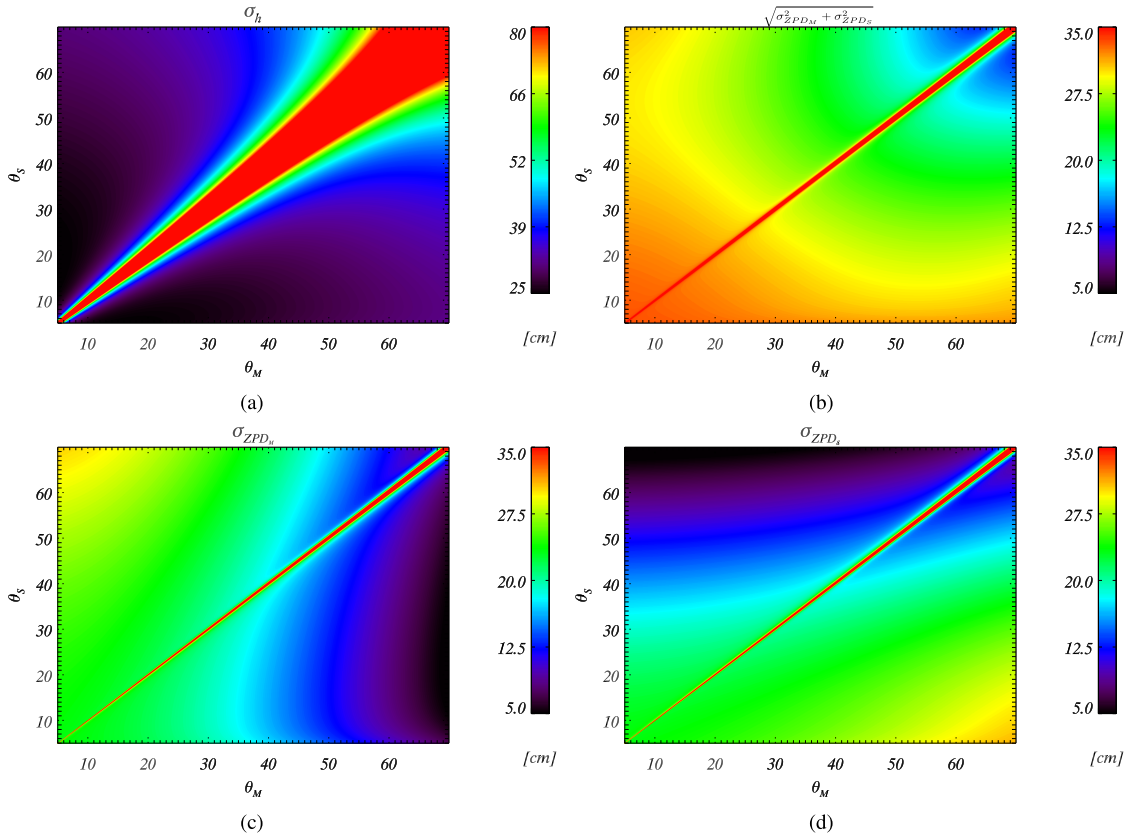

Fig. 4. Theoretical accuracies for different master and slave incidence angles assuming a target with 20-dB SCR. (a) Height accuracies. (c) and (d) ZPDs for master and slave acquisitions. (b) Combined error of both ZPDs.

TABLE II
PARAMETERS USED FOR MONTE CARLO SIMULATION OF TWO TARGETS FALLING WITHIN THE *"Fine Search of Candidates"*

SCR	$20\,dB$	$Num\ simulations$	10000
$\sigma_{ZPD_M}\ \&\ \sigma_{ZPD_S}$	$1.5\,cm$	θ_M	$54.7°$
σ_h^S	$9.31\,m$	θ_S	$36.1°$
A_{search}	$0.24\ m^2$	$\sigma_{h,ROI}$	$30\,m$

that just happens to be within the search area. The parameters used for the simulation are summarized in Table II.

Fig. 5 shows the histogram for the inversion residuals for the target corresponding to the correct match (black) and for a random target (red). The weighted residuals follow a Chi-square distribution with four degrees of freedom. For this example, the chances to pick the random target instead of the correct one are 21.3%. Note that the random target has to fall within the search area that has just 0.24 m². The target density plays an interesting role: on the one hand, it helps to reduce the fine search area by reducing the atmospheric error, and on the other hand, it increases the chances of having a wrong target within that area. It is difficult to give an accurate probability of correct matching. To study this topic in detail is out of the scope of this paper. In order to obtain an empirical evaluation, consider that in the example that we are going to present the target density is 0.2 targets per square meter. If we take the simulation parameters for all targets, a probability of wrong matching will be 2%. This does not include the targets that simply do not have a match due to the geometry change.
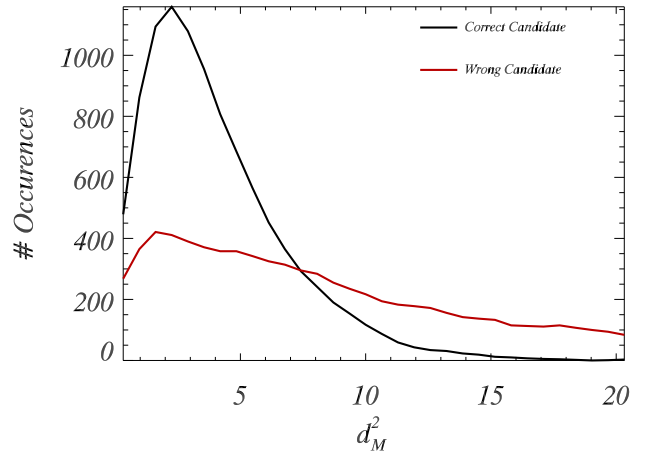

Fig. 5. Residuals histograms for a target corresponding to the correct match (black) and a random target (red).

In those cases, a random target may fall into the search area without having any "competitor" and be taken as a good one. All things considered, the probability of incorrect matching may be around a few percentage points.

V. RESULTS

A. Single-Image Processing Results

In this section, we present results over two different data sets using the single-image autofocus technique described earlier. The first results concern the reconstruction of a building facade in Berlin, Germany. The second one is the positioning of a well-characterized corner reflector (CR) in Wettzell, Germany.
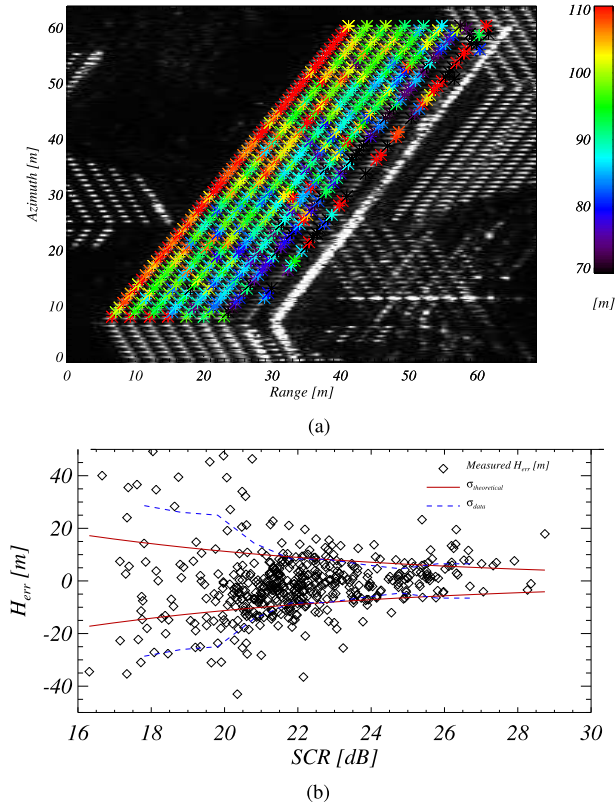
(a)

(b)

Fig. 6. Results over a facade in Berlin, Germany. (a) Obtained heights using the described autofocus method. (b) Statistics of the height estimation errors.

1) Building Facade: Our first results were obtained over a building facade in the city of Berlin, Germany ($52°31'54.4''N$ $13°22'38.5''E$). The height estimation of the scatterers on the facade was performed using a single TerraSAR-X ST acquisition (October 9, 2014). The incidence angle was 36.1° and the azimuth bandwidth was 38.3 kHz. Fig. 6 shows the results of the height estimation. The tropospheric delay was estimated using the European Center for Medium-Range Weather Forecasts model [24] and the corresponding height bias was removed accordingly. Fig. 6(a) shows the estimated heights plotted over the facade in the SAR image. Note that less points are selected for the lower part of the facade due to overlap with other scattering mechanisms from other facades. In general, these points do not pass the point target selection as they do not follow a clear "amplitude versus height processing pattern" like the one shown in Fig. 1(a). However, few points are close to show a pointlike target pattern and pass the test. Those points still contain valid information; they will just show a worse estimation as expected according to its SCR. The lower part of the facade in Fig. 6(a) shows some selected points that seem to have bigger errors due to some interference from nearby targets.

Fig. 6(b) displays the statistics of the discrepancies between the proposed method and heights derived from a Light Detection and Ranging (LiDAR) height map. Unfortunately, the LiDAR height maps provided only the ground height of the building, which we identified with the very strong double bounce in the SAR image. In order to derive validation heights for every selected SAR target on the facade, we have assumed

TABLE III
DISCREPANCIES BETWEEN THE AUTOFOCUS-BASED HEIGHT
AND THE GROUND TRUTH (GPS)

Date	θ_{inc}	$h_{found} - h_{GPS}$
2015 - 02 - 07	33.2°	−0.86 m
2015 - 02 - 08	54.1°	−3.54 m
2015 - 05 - 12	45.1°	3.40 m
2015 - 05 - 18	54.1°	1.44 m
2015 - 05 - 29	54.1°	2.92 m

the targets to be perfectly aligned and the building to be vertical. We, therefore, simply converted the range distance of each target from the double bounce and scaled it to a height by dividing by the cosine of the local incidence angle.

The standard deviation of the height as a function of SCR [the blue dotted line in Fig. 6(b)] showed a good agreement with the theoretical accuracy (20), represented by the red solid line. The bias between the obtained heights and the heights estimated from the Lidar DEM is −1.4 m; if it were because of a wrong ZPD estimation by the weather model, it would correspond to a ZPD error of 4.4 cm.

2) Wettzell Corner Reflector: The second example exploits the data of a controlled experiment with a CR deployed in Wettzell, Germany. This test scenario presents very accurate ground data. The corner is located next to a dedicated Geodetic Observatory station: accurate values of tropospheric and ionospheric delays were available for the image acquisition times, as well as precise Global Positioning System (GPS) monitoring of the CR itself. Moreover, the corner presents an SCR of 50 dB so that the corresponding height accuracy according to (20) is just 15 cm. Several images in ST mode were available over this test site. The acquisition of raw data was processed assuming different fixed heights and tropospheric delays at the sea level. The plot shown in Fig. 1 represents the amplitudes of the CR for different processing heights and tropospheric delays.

We analyzed five ST images in total. The acquisition dates, incidence angles, and differences with respect to on ground GPS measurements are summarized in Table III.

As it can be seen in Table III, the differences are significantly above the expected Cramér-Rao Lower Bound (CRLB) accuracy (15 cm). This means that there are effects that have not been taken into account. This kind of random error behavior may be related to FM rate error sources; further details are given in Appendix B.

B. Two-Image Processing Results

The facade shown in the previous results was also processed with the two-image algorithm and the results are presented in this section. First, we show the results of the joint ZPD estimation, the so-called "Step I." Then, we continue with "Step II" processing to absolute height retrieval.

1) Step I. Joint Estimation of ZPDs: In the two images, in our ROI, the slave acquisition presented an incidence angle $\theta_S = 36.1°$, whereas in the master acquisition, the incidence
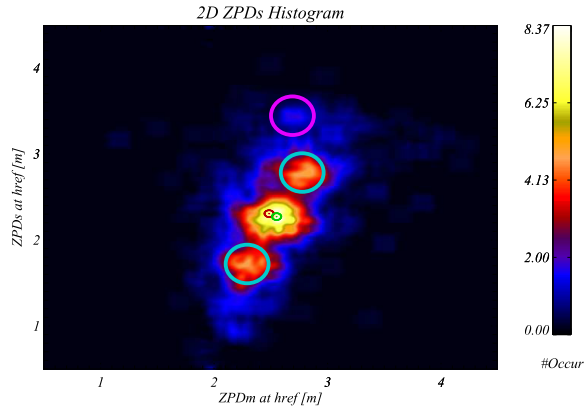
Fig. 7. 2-D histogram of ZPD at $h_{\rm ref}$ for master and slave acquisitions. The "large" circles highlight solution pairs outside the main peak, in particular, circles in turquoise define two other ambiguous distributions due to the facade regular pattern, whereas the purple marks define just some random solutions derived from wrong candidates. The "small" red circle represents the ZPD at $h_{\rm ref}$ estimated using weather models [24] and the "small" turquoise represents the values selected by the algorithm.

TABLE IV
ZPD AT HEIGHT REFERENCE ESTIMATED BY A WEATHER MODEL
AND THE DESCRIBED METHOD

	Weather Model	Our Method	Diff.
Master	2.31 m	2.28 m	2.2 cm
Slave	2.49 m	2.55 m	−6.4 cm

angle was $\theta_M = 54.7°$. Fig. 7 shows the 2-D histogram of ZPD at the reference height for master and slave acquisitions. The ZPD estimation was performed fitting iteratively a Gaussian probability density function to the 2-D solution space defined by the ZPDs of master and slave of each system of equations. In this case, the distribution is multimodal with three peaks, a consequence of the regular pattern of the targets in the facade. However, the iterative fitting progressively rejected the ambiguous solutions ending up selecting the peak with more energy.

The expected errors for a single system of equations, assuming 20-dB SCR, are: $\sigma_h = 32.7$ cm, $\sigma_{{\rm ZPD}_M} = 10.5$ cm, and $\sigma_{{\rm ZPD}_S} = 18.4$ cm. There are 497 points in the facade, so the joint estimation of the ZPDs should present a random error at the centimeter level. However, the theoretical systematic errors for this configuration are: $\sigma_{h,\rm sys} = 49.1$ cm, $\sigma_{{\rm ZPD}_M} = 12.2$ cm, and $\sigma_{{\rm ZPD}_S,\rm sys} = 8.1$ cm. The absolute height accuracy is below the meter level. Unfortunately, the accuracy of the retrieved ZPDs is in the order of few centimeters, which makes this estimation not useful for some applications such as the removal of atmospheric phase screen in SAR interferograms.

Table IV shows a good agreement between the ZPD estimated using the weather model and the described method.

As expected, the discrepancies are in the order of few centimeters due to the weather model centimeter accuracy and the ZPDs systematic errors. It is worth noticing that the case under study is particularly difficult because of the particular spatial alignment of the targets, corresponding to a repetition of the same elements on different floors [Fig. 8(a)].
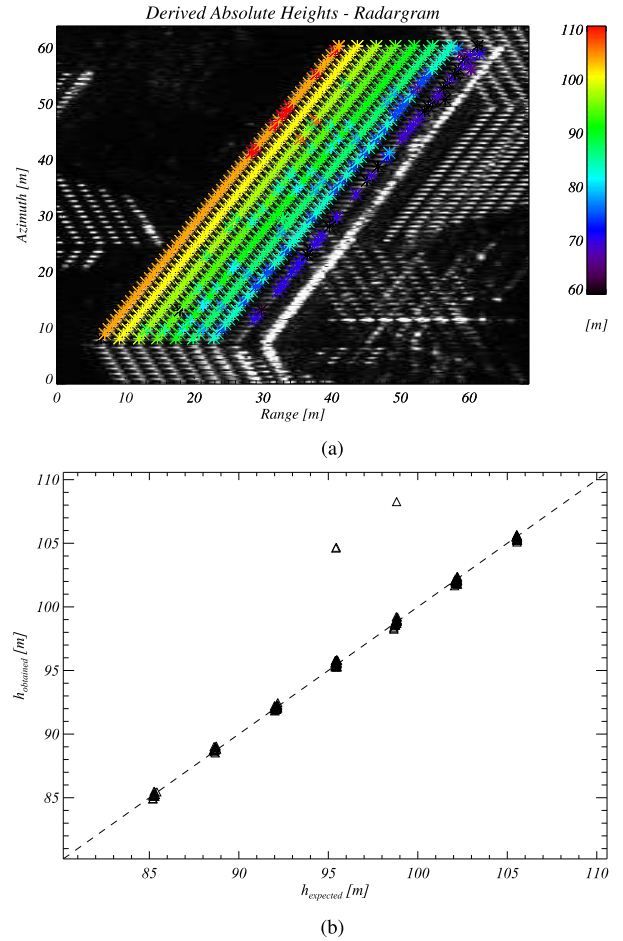

(a)

(b)

Fig. 8. (a) Obtained using the proposed method and (b) LiDAR comparison.

Normally, the expected 2-D histogram should present a single-peak distribution emerging above a noise floor (Fig. 7).

2) Step II. Absolute Height Estimation: In this section, we present the result of final height retrieval of the point targets located over the building facade shown in the previous example. The master and slave incidence angles had a difference of 18°. The heading angle difference between the master and slave acquisitions was 3.5°. A range and azimuth displacement of 1 m with respect to the expected position corresponds to a height offset of 1.9 and −12.37 m, respectively. The estimated ZPDs for this ROI have been presented in the previous step. At this point, we solved again a system of equations for each candidate pair, as explained in Section III-B, fixing the ZPDs estimated in the previous step. Finally, after the automatching process, the absolute heights were obtained for each target.

Fig. 8 shows the absolute heights over the facade (top), and a comparison with LiDAR measurements (bottom). It is clear that the height estimation improvement by using the described two-image processing with respect to the previous method using just one image (Fig. 6). The height bias is just −18.4 cm and the standard deviation is only 15.7 cm. The probability of detection is close to 90%, yielding a 10% false alarm rate.

VI. CONCLUSION

This paper has described an automatic target matching algorithm for two SAR acquisitions acquired under different

look and squint angles. The algorithm uses 3-D information contained in the curvature of the phase histories of point targets: this allows to limit the search area for target matching within a few square meters. The matching itself is based on the identification of ZPDs, exploiting their low-pass character in space. The final performance, assuming correct matching, depends on the geometric diversity of the two acquisitions and the SCR. The inversion allows to geolocate the targets and determines the ZPDs affecting each acquisition with decimetric and centimetric precisions, respectively; however, the accuracy is limited by the presence of biases. Possible physical explanations for the biases and their magnitudes are listed in the Appendix.

One could wonder whether target nonideality could be the reason for the unexplained errors, but this hypothesis is unlikely. On the one hand, the target in Wettzell is very close to being ideal; nonetheless, it presents discrepancies much larger than the theoretical accuracy. On the other hand, the Berlin test case shows that all targets share a large part of the error (hence the label of "bias"), whereas the extant part follows the theoretical accuracy dependent of the SCR.

The ST mode used in this paper has some limitations: for instance, the very limited along-track coverage. We show in the Appendix that three azimuth subbands would be enough to recover the curvature of the phase history and, hence, a good *a priori* for target matching.

We, therefore, propose a new acquisition mode consisting of three well-separated azimuth beams to avoid the necessity to operate a ST and the inherent coverage limitations. Since a SAR with two simultaneous azimuth beams has been described in [25] and was called BiDiSAR, we call this SAR mode with three azimuth beams a TriDiSAR. The three beams could be obtained in several ways: for instance, with three physical antennas on the same platform, or with a single antenna designed to radiate three main beams, or an antenna with azimuth scanning capabilities. An alternative concept would be having a small fleet of SAR satellites flying in close formation. A TriDiSAR will allow mapping precisely the position of point targets in large urban areas within days. With repeated acquisitions, one could easily detect changes, for instance, in rapidly developing areas or after a disaster. Such a mode will likely find additional applications that are beyond the scope of this paper.

The limited coverage of the current data notwithstanding, future work could be directed at recovering the tropospheric delay at image level and comparing it to numerical weather model predictions or atmospheric delays estimated from PSI.

APPENDIX

A. FM Rate Estimation Performance

In order to calculate the CRLB for the FM rate estimation, the phase signal model has to take into account two coupled parameters, a phase offset ϕ_0 (the zero-Doppler phase) and a curvature parameter K_r, i.e., the FM rate itself

$$\phi(t) = \phi_0 + \pi K_r t^2. \tag{13}$$

The Fisher information temporal density will be a matrix of 2×2 elements. The element (1, 1) is related to the derivatives

of $\phi(t)$ with respect to ϕ_0; the element (2, 2) with respect to K_r, and (1, 2) and (2, 1) are related to the cross derivatives

$$\mathbf{FIM}(t) = \frac{2\,\mathrm{SCR}}{T} \cdot \begin{pmatrix} 1 & \pi t^2 \\ \pi t^2 & \pi^2 t^4 \end{pmatrix}. \tag{14}$$

The integrated Fisher information over the entire aperture T will be

$$\mathbf{FIM} = \int_{-T/2}^{T/2} \mathbf{FIM}(t)dt. \tag{15}$$

Finally, the CRLB for the variance estimation of K_r is, therefore,

$$\mathrm{CRLB}_{K_r} = \frac{T}{2\,\mathrm{SCR}} \frac{\int 1\,dt}{\int 1\,dt \cdot \int \pi^2 t^4\,dt - \left(\int \pi t^2\,dt\right)^2}. \tag{16}$$

If only parts of the bandwidth are available, the integrals can be limited to those parts. This will be analyzed more in detail in Appendix C, where a different method associated with a novel acquisition mode will be presented. In the case of using the whole bandwidth, the CRLB is

$$\mathrm{CRLB}_{K_r} = \frac{90}{\pi^2\,T^4\,\mathrm{SCR}}. \tag{17}$$

This result is identical to the one derived in [26].

B. Height Estimation Using FM Rate Mismatch

A height offset between the height used in focusing and target's true height is linked to an FM rate mismatch assuming flat Earth in [27] as

$$\Delta K_r \approx \frac{2g_{\mathrm{Hs}}}{\lambda R_0} \cdot \Delta h \tag{18}$$

where λ is the wavelength, R_0 is the range at the closest approach, g_{Hs} is acceleration related to the gravity at satellite's height, and Δh is the height offset. If the Earth curvature is taken into account, the previous equation is modified as

$$\Delta K_r \approx \frac{2g_{\mathrm{Hs}}}{\lambda R_0} \cdot \frac{R_e}{R_e + H_s} \cdot \Delta h = \frac{2g_{\mathrm{Hs}}}{\lambda R_0} \cdot K_{\mathrm{curv}} \cdot \Delta h \tag{19}$$

where R_e is the Earth radius and H_s is the satellite's height, $H_s \approx 514$ km for TerraSAR-X. The new term introduced by the Earth curvature is collected in the parameter K_{curv}. Taking into account (17) and (19), the expected height standard deviation is

$$\sigma_{h,\mathrm{autofoc}} = \frac{2 \cdot V_s^4}{\lambda \cdot R_0 \pi \cdot B_{\mathrm{az}}^2 \cdot g_{\mathrm{Hs}} \cdot K_{\mathrm{curv}}} \cdot \sqrt{\frac{90}{\mathrm{SCR}}} \tag{20}$$

where V_s is the satellite's effective velocity. A set of defocusing sources are now described analyzing their impact on the estimation of targets heights using autofocus.

1) Effect of a Constant Tropospheric Delay: The impact of the tropospheric delay on SAR focusing can be divided into two effects: the group delay will move the signal to a later range bin, for which the processor that ignores or partially ignores the troposphere will use a different chirp rate; on the other hand, the phase delay will change during the aperture since the pulse will travel through variable sections of the troposphere. The following derivation shows how the two

effects are equal and have the same sign. The FM rate is well known and defined by

$$K_r = \frac{1}{2\pi} \frac{\delta^2 \phi(t)}{dt^2} \tag{21}$$

where $\phi(t)$ is the phase history. If the phase history is approximated by a Taylor of second order, the FM rate yields

$$K_r = \frac{2V_s^2}{\lambda R_0}. \tag{22}$$

The FM rate group delay variation for a certain unaccounted slant-range delay is obtained by deriving (21) with respect to range, it yields

$$\Delta K_{r,\text{group}} = \frac{2 \cdot V_s^2}{\lambda \cdot R_0^2} \cdot \text{SPD} \tag{23}$$

where SPD is the one-way slant path delay at zero Doppler. The processing chirp rate will be less negative than what it should be. The effect of the phase delay during the aperture due to troposphere is already analyzed in [28]–[30]. Here, we analyze the complete effect and link the total FM rate error with an introduced bias in the proposed height estimation. The target will have the following extra phase:

$$\psi(\Psi) = -\frac{4\pi}{\lambda} \frac{\text{SPD}}{\cos(\Psi)} \approx -\frac{4\pi}{\lambda} \text{SPD} \cdot \left(1 + \frac{\Psi^2}{2}\right) \tag{24}$$

where Ψ is the azimuth squint angle. The approximation is valid for small angles of Ψ, which is, in general, true for spaceborne SAR acquisitions. Thus, Ψ can be approximated as $\Psi = V_s \cdot t_{\text{az}}/R_0$, being t_{az} the azimuth time. The quadratic phase variation with respect to azimuth time yields

$$\psi(t_{\text{az}}) = -\frac{4\pi}{\lambda} \cdot \text{SPD} \cdot \frac{V_s^2}{2R_0^2} \cdot t_{\text{az}}^2. \tag{25}$$

Therefore, the azimuth chirp rate error is easily derived as

$$\Delta K_{r,\text{phase}} = \frac{2 \cdot V_s^2}{\lambda \cdot R_0^2} \cdot \text{SPD}. \tag{26}$$

Also, in this case, the processing will use an FM rate that is less negative than it should be. Then, the total FM error is

$$\Delta K_{r,\text{total}} = \frac{4 \cdot V_s^2}{\lambda \cdot R_0^2} \cdot \text{SPD}. \tag{27}$$

The height bias can be deduced putting (19) and (27) together as

$$\begin{aligned}
\Delta h_{\text{tropo,bias}} &= \frac{2 \cdot V_s^2}{g_{\text{Hs}} R_0 \cdot K_{\text{curv}}} \cdot \text{SPD} \\
&\approx \frac{2 \cdot V_s^2}{g_{\text{Hs}} R_0 \cdot K_{\text{curv}}} \cdot \frac{\text{ZPD}}{\cos(\theta_{\text{inc}})} \\
&\approx \kappa \cdot \text{ZPD}
\end{aligned} \tag{28}$$

where all the parameters multiplying the ZPD are collected in κ. Here, the SPD has been projected in the ZPD taking into account the incidence angle θ_{inc}.

2) Effect of a Constant Ionospheric Delay: Regarding the ionospheric effect, it also presents group and phase delays. The group delay has the same effect as in the troposphere (23); it will make the phase history excessively curved for the range bin in which the signal will appear. However, the phase will now advance, opposite to the group delay, by the same amount. This is because the ionosphere has the effect of advancing phases, while it delays wave envelopes. The final result would be that the target will be properly focused, though appearing in the wrong range position.

3) Orbit Errors and the FM Rate: Since the measurement of the slant range is intrinsically correct (neglecting other delays), what changes in case of incorrect positioning of the platform are the assumed incidence angle. Then, the introduced height bias is related to the range orbit error as

$$\Delta h_{\text{rg-orb,bias}} = \Delta R_{\text{orb}} \cdot \cos(\theta_{\text{inc}}). \tag{29}$$

This means that a constant orbit error for the aperture introduces a bias in height in the same order of magnitude. Thus, for TerraSAR-X where the orbit error is in the order of few centimeters, the introduced height error can be neglected. For the sake of completeness, the bias due to orbit errors analyzed in [21] would be valid if the complete orbit was corrected using a target on the ground and its GPS position is worth mentioning.

4) Nonlinear Effects: Up until now, it has been discussed what happens when there is some constant effect during the whole aperture. An orbit range offset introduces a height estimation error similar to the range offset magnitude. In that case, the assumed target phase history presents just an offset for the whole aperture versus the true one. For a constant unaccounted tropospheric delay, the phase history has an extra quadratic term that implies in an FM rate mismatch, and therefore, it has the same effect as height offset assumed in focusing. Let us assume now that the tropospheric ZPD is composed by a constant value and a quadratic term depending on the squint angle,

$$\text{ZPD}(\Psi) = K + \gamma \cdot \Psi^2. \tag{30}$$

The effect is illustrated in Fig. 9, in which the group delay is given by the average of (30), which is depicted in this figure as $\text{ZPD}_{\text{ct,equ}}$.

However, there is an extra term of FM rate mismatch due to the phase introduced by the quadratic behavior of the ZPD. This term can be approximated taking into account second-order phase terms as

$$\Delta K_{r,\text{phase}}^{\text{high}} = \frac{4 \cdot V_s^2}{\lambda \cdot R_0^2} \cdot \gamma. \tag{31}$$

Thus, the relationship between the quadratic ZPD term and height offset is defined as

$$\Delta h_{\text{tropo,bias}}^{\text{high}} = \frac{2 \cdot V_s^2}{g_{\text{Hs}} R_0 \cdot K_{\text{curv}}} \cdot \gamma. \tag{32}$$

One may think in the first place that this term could be negligible. However, if some reasonable values are set, it is possible to observe that a few meters bias can be likely produced by a nonconstant troposphere. Let us see, for example, what would produce 1-m bias. Some reasonable parameters taking
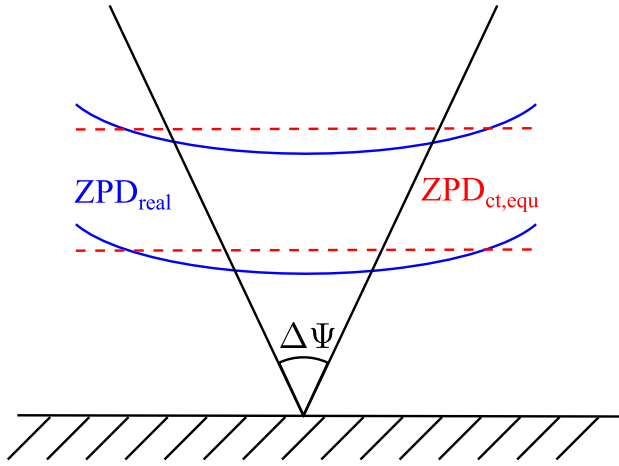
Fig. 9. Quadratic ZPD during the illumination time (ZPD_real) and equivalent constant ZPD ($\text{ZPD}_\text{ct,equ}$).

into account the TerraSAR-X mission are $V_s = 7600$ m/s, $g_\text{Hs} = 8.6$ m/s^2, $R_0 = 605$ km, and $K_\text{curv} = 0.92$. Therefore, the needed γ to produce 1-m bias is $\gamma = 0.04$ m/rad^2. If we take into account ST acquisition, this γ value corresponds to zenith delay variations at the edge of the aperture with respect to the center of only 0.06 mm. Assuming a single-layer model located at 6 km height, the horizontal extension seen by the total aperture is 460 m. Therefore, it can be said that with the assumed reasonable parameters, a variation of the ZPD of 0.06 mm within 230 m would cause the same effect in range history as 1-m-height focus bias. The derived number is actually very small and seems hard to be achieved. Nevertheless, one should consider that below 2 km, the troposphere behaves with a smoother regime (8/3 spectral index [22]) making the related delay much more correlated inside the synthetic aperture. This topic requires, indeed, some dedicated research work addressing a deeper understanding of the behavior of the tropospheric turbulence on the kilometer scale: in particular, the spectral index as mentioned before and the effective height of the turbulence (probably lower than 6 km) that would also determine the degree of spatial correlation of the measurements.

The same effect would be present in the case of quadratic error in the orbit trajectories. In the case of the ionospheric delay, as it has been demonstrated, the constant part would cancel out taking into account the group and phase delay. However, if the ionospheric zenith delay can be projected on a second-order polynomial, it would have again the same effect as a height focus bias. The delay produced by ionosphere can be expressed as [31]

$$\Delta R_\text{iono} = \frac{2K}{f_0^2} \cdot \frac{\text{TEC}}{\cos(\theta_\text{inc})} \tag{33}$$

where $K = 40.3$ m^3/s^2, TEC refers to the vertical total electron content, and f_0 is the carrier frequency. Thus, taking into account TerraSAR-X carrier frequency of 9.65 GHz and assuming an incidence angle of 33°, a variation of 0.06 mm corresponds to a vertical TEC variation of just 0.006 TECU (1 TECU $= 10^{16}$TEC). Therefore, taking into account these numbers, small unaccounted (or not measurable)

variations within the aperture provoke a bias in our estimation in the order of few meters. The method proposed using two images is much more robust to this kind of effect.

C. Efficient Processing

A constraint of the proposed method is the need for long SAR apertures, which are necessary to get enough accuracy in the height estimation using a single image. However, this normally entails a reduced area on the ground, such as for the TerraSAR-X ST acquisition mode. In this section, we discuss briefly an autofocusing method based on three separated azimuth beams and its performance. This analysis allows predicting the performance of a TriDiSAR, a stripmap mode with three azimuth beams.

The estimation of the FM rate (K_r) for the single-image height determination might be done in a different way from what proposed in Appendix B. The aim is to estimate the second derivative of the residual phase history, which can be done using the phases of three looks: two at the sides of the aperture and one at the center. Let us call them ϕ_{-1}, ϕ_0, and ϕ_{+1}. The filter coefficients for the curvature estimation would be $(1, -2, 1)$ to be divided by the square of the time separation ΔT. Explicitly

$$\hat{K}_r = \frac{\phi_{-1} - 2\phi_0 + \phi_{+1}}{2\pi (\Delta T)^2}. \tag{34}$$

Considering that the middle look is used twice, its support should be longer to avoid that its noise contribution dominates the performance: for instance, one can take three subapertures with durations $T/6$, $T/3$, and $T/6$. Unfortunately, the proposed estimator is biased because of the phase curvature within each look; the bias depends on the frequency extent of the looks. With the proposed subaperture lengths, the estimator bias is

$$\text{E}[\hat{K}_r - K_r] = \frac{1}{(\pi \Delta T)^2} \left[\int_{-T/12}^{T/12} \pi K_r t^2 - \int_{-T/6}^{T/6} \pi K_r t^2 \right]$$
$$= -\frac{7}{450} K_r \tag{35}$$

and we would rather use the unbiased estimator

$$\hat{K}_r' = \alpha \hat{K}_r \qquad \alpha = \frac{1}{1 - 7/450}. \tag{36}$$

Compared to the full bandwidth, the SCR is six times worse for the side looks, compared to the full bandwidth, and only three times worse for the central one. One obtains for the variance of the unbiased estimator $\hat{K}_r'$

$$\text{Var}[\hat{K}_r'] \approx \frac{1}{2\pi^2 \, \text{SCR}} \frac{6 + 4 \cdot 3 + 6}{4(1/2 - 1/12)^4 T^4} \alpha^2 \approx \frac{102.70}{\pi^2 T^4 \, \text{SCR}}. \tag{37}$$

This result is still close enough to the CRLB (17): this simplified processing has acceptable performance but requires only one focusing run.

REFERENCES

[1] G. L. Prade, "An analytical and experimental study of stereo for radar," *Photogramm. Eng.*, vol. 29, no. 2, pp. 294–300, 1963.
[2] G. Gracie, R. K. Brewer, J. W. Bricker, and R. A. Johnson, "Stereo radar analysis," Raytheon Company, Alexandria, VA, USA, Tech. Rep. FTR-1339-1, May 1970.

[3] F. Leberl, "Accuracy analysis of stereo side looking radar," *Photogramm. Eng. Remote Sens.*, vol. 45, no. 8, pp. 1083–1096, 1979.

[4] M. Marra, K. E. Maurice, D. C. Ghiglia, and H. G. Frick, "Automated DEM extraction using RADARSAT ScanSAR stereo data," in *Proc. IEEE Geosci. Remote Sens. Symp. (IGARSS)*, vol. 5, Seattle, WA, USA, Jul. 1998, pp. 2351–2353.

[5] T. Toutin, "Stereo-mapping with SPOT-P and ERS-1 SAR images," *Int. J. Remote Sens.*, vol. 21, no. 8, pp. 1657–1674, 2000.

[6] D. Massonnet and T. Rabaute, "Radar interferometry: Limits and potential," *IEEE Trans. Geosci. Remote Sens.*, vol. 31, no. 2, pp. 455–464, Mar. 1993.

[7] R. Bamler and P. Hartl, "Synthetic aperture radar interferometry," *Inverse Problems*, vol. 14, no. 4, pp. 1–55, 1998.

[8] D. Just and R. Bamler, "Phase statistics of interferograms with applications to synthetic aperture radar," *Appl. Opt.*, vol. 33, no. 20, pp. 4361–4368, 1994.

[9] A. Ferretti, C. Prati, and F. Rocca, "Permanent scatterers in SAR interferometry," *IEEE Trans. Geosci. Remote Sens.*, vol. 39, no. 1, pp. 8–20, Jan. 2001.

[10] D. Perissin and F. Rocca, "High-Accuracy Urban DEM Using Permanent Scatterers," *IEEE Trans. Geosci. Remote Sens.*, vol. 44, no. 11, pp. 3338–3347, Nov. 2006.

[11] D. Small, A. Schubert, B. Rosich, and E. Meier, "Geometric and radiometric correction of ESA SAR products," in *Proc. Envisat Symp.*, Montreux, Switzerland, 2007, pp. 23–27.

[12] P. Capaldo, M. Crespi, F. Fratarcangeli, A. Nascetti, and F. Pieralice, "High-resolution SAR radargrammetry: A first application with COSMO-SkyMed SpotLight imagery," *IEEE Geosci. Remote Sens. Lett.*, vol. 8, no. 6, pp. 1100–1104, Nov. 2011.

[13] K. Goel and N. Adam, "Three-dimensional positioning of point scatterers based on radargrammetry," *IEEE Trans. Geosci. Remote Sens.*, vol. 50, no. 6, pp. 2355–2363, Jun. 2012.

[14] D. Li and Y. Zhang, "A rigorous SAR epipolar geometry modeling and application to 3D target reconstruction," *IEEE J. Sel. Topics Appl. Earth Observ. Remote Sens.*, vol. 6, no. 5, pp. 2316–2323, Oct. 2013.

[15] K. Gutjahr, R. Perko, H. Raggam, and M. Schardt, "The epipolarity constraint in stereo-radargrammetric DEM generation," *IEEE Trans. Geosci. Remote Sens.*, vol. 52, no. 8, pp. 5014–5022, Aug. 2014.

[16] A. Schubert, D. Small, M. Jehle, and E. Meier, "COSMO-Skymed, TerraSAR-X, and RADARSAT-2 geolocation accuracy after compensation for earth-system effects," in *Proc. IEEE Int. Geosci. Remote Sens. Symp.*, Jul. 2012, pp. 3301–3304.

[17] M. Eineder, C. Minet, P. Steigenberger, X. Cong, and T. Fritz, "Imaging geodesy—Toward centimeter-level ranging accuracy with TerraSAR-X," *IEEE Trans. Geosci. Remote Sens.*, vol. 49, no. 2, pp. 661–671, Feb. 2011.

[18] C. Gisinger *et al.*, "Precise three-dimensional stereo localization of corner reflectors and persistent scatterers with TerraSAR-X," *IEEE Trans. Geosci. Remote Sens.*, vol. 53, no. 4, pp. 1782–1802, Apr. 2015.

[19] A. Schubert, N. Miranda, D. Geudtner, and D. Small, "Sentinel-1A/B combined product geolocation accuracy," *Remote Sens.*, vol. 9, no. 6, p. 607, 2017.

[20] X. X. Zhu, S. Montazeri, C. Gisinger, R. F. Hanssen, and R. Bamler, "Geodetic SAR tomography," *IEEE Trans. Geosci. Remote Sens.*, vol. 54, no. 1, pp. 18–35, Jan. 2016.

[21] S. Duque, H. Breit, U. Balss, and A. Parizzi, "Absolute height estimation using a single TerraSAR-X staring spotlight acquisition," *IEEE Geosci. Remote Sens. Lett.*, vol. 12, no. 8, pp. 1735–1739, Aug. 2015.

[22] R. F. Hanssen, *Radar Interferometry: Data Interpretation and Error Analysis*, vol. 2. Dordrecht, The Netherlands: Springer, 2001.

[23] U. Balss, C. Gisinger, X. Y. Cong, R. Brcic, S. Hackel, and M. Eineder, "Precise measurements on the absolute localization accuracy of TerraSAR-X on the base of far-distributed test sites," in *Proc. 10th Eur. Conf. Synth. Aperture Radar (EUSAR)*, Berlin, Germany, Jun. 2014, pp. 1–4.

[24] X. Y. Cong, U. Balss, M. Eineder, and T. Fritz, "Imaging geodesy—Centimeter-level ranging accuracy with TerraSAR-X: An update," *IEEE Geosci. Remote Sens. Lett.*, vol. 9, no. 5, pp. 948–952, Sep. 2012.

[25] J. Mittermayer, S. Wollstadt, P. Prats-Iraola, P. Lopez-Dekker, G. Krieger, and A. Moreira, "Bidirectional SAR imaging mode," *IEEE Trans. Geosci. Remote Sens.*, vol. 51, no. 1, pp. 601–614, Jan. 2013.

[26] J. F. Green and C. J. Oliver, "The limits on autofocus accuracy in SAR," *Int. J. Remote Sens.*, vol. 13, no. 14, pp. 2623–2641, 1992.

[27] M. Rodriguez-Cassola *et al.*, "Doppler-related distortions in TOPS SAR images," *IEEE Trans. Geosci. Remote Sens.*, vol. 53, no. 1, pp. 25–35, Jan. 2015.

[28] M. Rodriguez-Cassola, P. Prats-Iraola, M. Jäger, A. Reigber, and A. Moreira, "Estimation of tropospheric delays using synthetic aperture radar and squint diversity," in *Proc. IEEE Int. Geosci. Remote Sens. Symp. (IGARSS)*, Melbourne, VIC, Australia, Jul. 2013, pp. 4491–4494.

[29] P. Prats-Iraola *et al.*, "On the processing of very high resolution spaceborne SAR data," *IEEE Trans. Geosci. Remote Sens.*, vol. 52, no. 10, pp. 6003–6016, Oct. 2014.

[30] G. Krieger, F. De Zan, M. Bachmann, J. H. Gonzalez, M. R. Cassola, and M. Zink, "Unexpected height offsets in TanDEM-X: Explanation and correction," in *Proc. IEEE Int. Geosci. Remote Sens. Symp.*, Jul. 2012, pp. 295–298.

[31] N. Jakowski, C. Mayer, M. M. Hoque, and V. Wilken, "Total electron content models and their use in ionosphere monitoring," *Radio Sci.*, vol. 46, no. 6, 2011, Art. no. RS0D18.

Sergi Duque received the B.S. degree in telecommunication engineering from the Polytechnic University of Catalonia (UPC), Barcelona, Spain, in 2005.

He was with UPC until 2011, where he was involved in bistatic synthetic aperture radar (SAR) and SAR interferometry. In 2008, he was with the University of Michigan, Ann Arbor, MI, USA, as a Visiting Researcher, where he was involved in 3-D bistatic SAR image focusing. In 2012, he joined the German Aerospace Agency, Weßling, Germany, as a Researcher for the bistatic German bistatic SAR satellite mission TanDEM-X. Since 2016, he has been with Magna Electronics, where he has been involved in automotive radar algorithm development. He has co-authored a pending European patent. His research interests include bistatic SAR interferometry, absolute SAR ranging, differential SAR interferometry, SAR tomography, SAR focusing, and automotive radar signal processing.

Mr. Duque was a recipient of the Second Prize of the X Premio Rosina Ribalta given by the EPSON Foundation to the Best National Thesis Proposals in the field of information and communication technologies in 2008.

Alessandro Parizzi received the master's degree in telecommunications engineering from the Politecnico di Milano, Milan, Italy, in 2004.

From 2004 to 2006, he was with the Department of Electronics, Politecnico di Milano, where he was involved in the field of synthetic aperture radar (SAR) interferometry. Since 2006, he has been with the Remote Sensing Technology Institute, German Aerospace Center (DLR), Weßling, Germany, where he has been involved in interferometric SAR processing. His research interests include the study of SAR interferometric processing and applications.

Francesco De Zan was born in Lodi, Italy, in 1979. He received the master's degree in telecommunications engineering, with a focus on signal processing and remote sensing, and the Ph.D. degree, with a focus on synthetic aperture radar (SAR) interferometry with distributed and decorrelating scatterers, from the Politecnico di Milano, Milan, Italy, in 2004 and 2008, respectively.

He has contributed to the development of the Terrain Observation with Progressive Scan acquisition mode, which is currently used on ESA Sentinel-1 satellites, and collaborated with T.R.E., Milan. In 2007, he joined the Stanford Exploration Group, Stanford University, Stanford, CA, USA, as a Visiting Researcher. In 2008, he joined the German Aerospace Center, Weßling, Germany, where he was with the Microwave and Radar Institute and then with the Remote Sensing Technology Institute, contributing to the development of the Tandem-L mission concept. He was involved in aspects related to acquisition planning, performance models for deformation retrieval with InSAR and SAR tomographic applications, orbit design, the calibration of the TanDEM-X interferometer, and discovering and explaining interferometric effects that were hampering the quality of the DEM products. He was also involved in several projects for the European Space Agency related to mission design, commissioning, and application development for SAR satellites. His research interests include SAR including the performance of phase and delay estimators, ionospheric propagation estimation, focusing and precise geolocation of targets, soil moisture and vegetation effects, and inconsistencies in SAR interferometric phases.